Amplifying photoreduction efficacy of Bi-Sb bimetallic nanocrystals: Manipulating carrier dynamics to boost CO_2-to-CO conversion

Jie Tian [a,c], Zhijian Wang [b,c], Yaqin Hou [a,c,*], Yatao Yang [a,c], Haijun Chen [d], Zhanggen Huang [a,c,e,*]

[a] *State Key Laboratory of Coal Conversion, Institute of Coal Chemistry, Chinese Academy of Sciences, Taiyuan, Shanxi 030001, China*
[b] *Key Laboratory of Carbon Materials, Institute of Coal Chemistry, Chinese Academy of Sciences, Taiyuan, Shanxi 030001, China*
[c] *University of Chinese Academy of Sciences, Beijing 100049, China*
[d] *Tianjin Key Laboratory of Optoelectronic Thin Film Devices and Technology, College of Electronic Information and Optical Engineering, Nankai University, Tianjin 300350, China*
[e] *Dalian National Laboratory for Clean Energy, Dalian, Liaoning 116023, China*

ARTICLE INFO

ABSTRACT

Inorganic Bi-based halide perovskites have attracted significant attention in the field of CO_2 photoreduction due to their excellent optoelectronic conversion performance and low toxicity. However, the inherent strong localization of electron-hole pairs remains the main factors limiting charge carrier transport and CRR performance. In this work, CBSB-x NCs with different Bi/Sb ratios were synthesized assisted by ultrasound methods to manipulate carrier behavior and assess CRR performance. The photoelectrochemical properties revealed that incorporation of Sb effectively suppressed nonradiative recombination and improved transport efficiency of charge carriers. Among the bimetallic variants, CBSB-1 NCs exhibited enhanced catalytic performance in CO production, with a yield of 38.77 $\mu mol\cdot g^{-1}$ and a high selectivity of 96.53 %. In-situ DRIFTS and DFT calculations indicated that Sb as co-catalytic sites promote charge transfer at the Bi-Br-Sb interface, accelerate the rapid evolution of b-CO_3^{2-} to HCOO⁻ and significantly reduce the reaction energy barrier of CO.

1. Introduction

The combustion of fossil fuels and carbon dioxide (CO_2) emissions have been identified as major contributors to severe resource depletion and climate change [1,2]. As a sustainable energy source, solar energy is deemed an optimal solution to alleviate energy and environmental crises by driving the conversion of CO_2 into high-value low-carbon fuels to form a closed carbon chain cycle [3–6]. Nevertheless, Photocatalytic CO_2 reduction reaction (CRR) remains an immensely challenging reaction in both thermodynamics and kinetics [7]. On one hand, the activation and conversion of CO_2, being the highest oxidation state of carbon and involving the energetically demanding C=O bond (750 kJ/mol), necessitate efficient catalysts and substantial energy input [8]. On the other hand, the photocatalytic CRR pathway entails sluggish multi-electron reaction kinetics, where the carrier dynamics of catalysts (such as carrier lifetime and transfer rate), dominate the population of photoexcited carriers participating in interfacial reactions, further leading to variations in photocatalytic rates [9]. The majority of efforts

have faced the dilemma of reconciling these two aspects, resulting in unsatisfactory photoreduction efficiency and selectivity, which propelling the proactive design and development of innovative photocatalytic materials.

Metal halide perovskites (MHPs), with band positions meeting the thermodynamic requirements for H_2O and CO_2 reduction, and continuous ion layers effectively shortening the charge transfer distance, find applications in photocatalytic CRR [10,11]. Bismuth (Bi)-based MHPs (such as $Cs_3Bi_2X_9$) are regarded as potential candidates for CO_2 photoreduction due to their superior photocatalytic performance while overcoming the environmental toxicity and inherent instability limitations of lead-based MHPs [12,13]. Recent advancements have demonstrated that the nanostructured assembly of Bi-based MHPs exhibit reduced defect density at grain boundaries and surfaces, attributed to interface effects and quantum confinement, thereby minimizing carrier recombination [14,15]. Furthermore, the low-dimensional structures exhibit pronounced suppression of ion migration owing to their higher ion activation energy and truncation effects [16]. However, the strong

---

localization of electron-hole pairs is amplified in low-dimensional materials, resulting in restricted charge transfer in the vicinity of Bi [17]. The high electron cloud density around Bi is the main factor contributing to the minimum conduction band of Bi based MHPs due to the contribution of Bi's 6p orbital, which further establishes Bi as a persistent adsorption site for Bi based MHPs CRR [18].

Although most reaction mechanisms are based on localized reaction mechanisms occurring at individual active sites, the electron delocalization mechanism suggests that the migration of electrons between active sites can effectively reduce the activation energy of the reaction and accelerate the reaction rate [19]. Given the flexibility and tunability of MHPs structures, ions incorporation or alloying strategies are convenient and effective treatments to reduce the strong localization of electron-hole pairs [20]. Not only can the local electric field and charge distribution be improved by adjusting the charge state and electronic state density, but also the thermodynamic efficiency for CRR can be enhanced by modulating band structure via introduction of additional electronic states and providing new active site [21]. However, the corresponding alloyed perovskites are currently underinvestigated, and the catalytic mechanism in the realm of CRR is still elusive, rendering the achievement of these strategies through structural modulation of photocatalysts a challenging endeavor.

In this study, antimony (Sb), with similar electronic structure (5 $s^2 5p^3$) and chemical characteristics to Bi (6 $s^2 6p^3$), was incorporated into $Cs_3Bi_2Br_9$ perovskite, and due to its similar electronic structure and chemical properties to bismuth, it did not significantly alter the stability of the octahedral structure of $Cs_3Bi_2Br_9$. The improved Bi-Br-Sb asymmetric configuration can improve the adsorption energy of CO_2 by reducing the p-band center of Br to build Br sites, and promote the further rapid activation of CO_2 by increasing the delocalized charges around Bi sites. Photophysical characterization revealed that presence of Sb effectively reduced bandgap and defect density, suppressed non radiative recombination, and improved charge mobility. In situ diffuse reflectance infrared Fourier transform spectroscopy (DRIFTS) and density functional theory (DFT) have elucidated that Sb serves as a pivotal co-catalytic site, fostering the swift kinetic evolution of bidentate carbonate (b-CO_3^{2-}) and substantially diminishes the energy barrier for carbon monoxide (CO) production. Through reasonable optimization of thermodynamics and kinetics, $Cs_3BiSbBr_9$ (CBSB-1) exhibits enhanced CO conversion rate and selectivity. This work has experimental and theoretical significance for the research and development of perovskite CRR catalysts.

2. Experimental procedures

2.1. Materials

All materials were used without further purification, caesium bromide (CsBr, 99.5 %, Macklin), bismuth bromide (BiBr$_3$, ≥98 %, Aladdin), antimony bromide (SbBr$_3$, 99.9 %, Aladdin), N, N-dimethylformamide (DMF, AR, ≥99.5 %, Aladdin), isopropyl alcohol (AR, ≥99.7 %, DAMAO), hexane (AR, ≥99.5 %, Kermel).

2.2. Synthesis of Cs₃Bi₂₋ₓSbₓBr₉ Nanocrystals (NCs)

$Cs_3Bi_{2-x}Sb_xBr_9$ NCs (x = 0, 0.5, 1, 1.5, 2) were synthesized by ultrasound-assisted antisolvent recrystallization strategy and denoted as CBB, CBSB-0.5, CBSB-1, CBSB-1.5, CSB, respectively [12,22]. For CBB NCs, 0.3 mmol CsBr and 0.2 mmol BiBr$_3$ were added to 5 mL N, N-dimethylformamide (DMF), and ultrasonic at 120 W for 1 h until sufficiently dissolved to form a precursor solution. 1 mL of precursor was quickly injected into 30 mL of isopropanol during vigorous stirring, and continued stirring for 1 min. The obtained solution was centrifuged at 3000 rpm for 3 min to remove large particles and then centrifuged at 8000 rpm for 5 min to discard the supernatant. The precipitate was washed three times with n-hexane to finally obtain CBB NCs. CBSB-*x* and

CSB were synthesized in a similar way by adjusting the ratio of BiBr$_3$ and SbBr$_3$.

2.3. Characterizations

The transmission electron microscopy (TEM) images and EDS spectra were characterized by JEOL JEM-F200 and JED-2300 T, respectively. The powder X-ray diffraction (XRD) patterns were measured by SmartLab-9 from Rigaku corporation with Cu-Kα radiation (λ = 0.15416 nm) at 40 kV and 40 mA. The X-ray photoelectron spectroscopy (XPS) spectra and valence-band (VB) XPS spectra were measured on Escalab 250Xi from Thermo Fisher Scientific equipped with an Al Ka radiation source. Ultraviolet-visible diffuse reflection spectra (UV–vis DRS) were obtained by UV270 from SHIMADZU at the range of 200–800 nm. Time-dependent photocurrent curves were conducted on CHI-660D electrochemical workstation with Pt slice as the counter electrode, Ag/AgCl (saturated KCl) as the reference electrode, photocatalyst loaded FTO glass as the working electrode, and ethyl acetate dissolved 0.1 M tetrabutylammonium hexafluorophosphate (TBAPF$_6$) as the electrolyte. Photoluminescence spectroscopy (PL) spectra and time-resolved photoluminescence spectroscopy (TRPL) spectra were characterized by the Hamamatsu C11347–11 fluorescence spectrometer under the excitation wavelength of 410 nm. The electron paramagnetic resonance (EPR) spectra were recorded by Bruker A300 instrument.

2.4. Photocatalytic CO₂ reduction

The photocatalytic CO$_2$ reaction consists of a 300 W xenon lamp illumination system (Perfect light PLS-SXE300) equipped with an AM 1.5 G filter, a 50 mL offline quartz reactor, and a gas chromatograph (GC-2014, Shimadzu) equipped with a flame ionized detector (FID) and a thermal conductivity detector (TCD). Specifically, 10 mg photocatalyst was ultrasonically dispersed in 1 mL toluene and evenly spread onto a glass fiber filter membrane with a specific diameter (25 mm) and pore size (0.45 μm), and dry at 80 °C for 30 min to remove excess dispersant. Subsequently, the glass fiber filter membrane loaded with photocatalyst was transferred to the glass support inside the reactor. Before lighting, the reactor containing 100 μL H$_2$O was degassed to vacuum repeatedly, and filled with high-purity CO$_2$ (99.99 %) to 101kPa. During the reaction process, a 25 ± 0.01 °C circulating water bath was used to eliminate thermal radiation, and gaseous products were evaluated using the GC-2014.

2.5. In-situ DRIFTs measurements

In-situ DRIFTS measurements are taken on Bruker's Tensor 27 in situ infrared spectrometer. Before adsorption, the sample was purged with 50 mL·min^{-1} Ar at 100 °C for 30 min to remove surface impurities. The background spectrum was collected after the temperature of the reaction tank dropped to 25 °C. Then, the mixed reaction airflow containing 25 mL·min^{-1} Ar, 5 mL·min^{-1} and a trace amount of water was introduced into the reaction tank in the dark, and the change of FTIR spectra with time was recorded for 10 min, and the background spectrum was collected again after the reaction. Subsequently, a 300 W xenon lamp with an AM 1.5 G filter was turned on to investigate the intermediates under simulated sunlight, and the FTIR spectra were continuously monitored for 60 min

2.6. Computational methodology

The quantum chemical calculation was carried out in the DMol3 module of Material Studio. The generalized gradient approximation (GGA) with Perdew – Burke-Ernzerhof (PBE) theory and all-electron dual numerical value with polarization function (DNP) was applied. For geometric optimization, convergence tolerances for energy, maximum force, and maximum displacement are 1.0×10^{-5} Ha, $2.0 \times$

10^{-3} Ha/ Å, and 5.0×10^{-3} Å, respectively. Monkhorst-Pack K points grid was set to $3 \times 3 \times 1$. The Grimme method for DFT-D correction is taken into account in all calculations. The periodic four-layer plate models with p (2×2) cells were used to simulate the (-101) surface of $Cs_3Bi_{2-x}Sb_xBr_9$. The vacuum layer of cells was set to 20 Å to avoid the interaction between adjacent layers, and the bottom two layers of the cell atoms were fixed, the rest of the atoms were relaxed. The adsorption energies of absorbate on the substrate (ΔE_{ads}) were calculated by equation $\Delta E_{ads} = E_{ABS@CAT} - E_{CAT} - E_{ABS}$, where $E_{ABS@CAT}$, E_{CAT}, and E_{ABS} are the energy of the catalyst associated with absorbate, catalyst and absorbate molecules, respectively. The Gibbs free energies (ΔG) of each reaction step were calculated at 298.15 K by the equation $\Delta G = \Delta E_{ads} + \Delta E_{ZPE} - T\Delta S$, where ΔE_{ZPE} and $T\Delta S$ are the zero-point energy change and entropy change, respectively.

3. Results and discussion

3.1. Synthesis and structural characterization of CBSB-x

The morphologies and particle size distributions of CBB, CBSB-1, and CSB under transmission electron microscopy (TEM) are shown in Fig. 1 (a-c). It can be seen that CBB, CBSB-1, and CSB present dispersed and uniform nanocrystals, and the average particle size decreases slightly with the Sb^{3+} doped, which is 5.85 nm, 5.76 nm, and 5.72 nm, respectively. The fast Fourier transformation (FFT) was applied to high resolution transmission electron microscopy (HRTEM) to calculate the lattice spacing (Fig. S1). The identical (210) lattice planes assigned to CBB, CBSB-1, and CSB in all cases correspond to slightly reduced lattice spacing of 0.28 nm, 0.27 nm, and 0.27 nm, respectively, which can be attributed to the contraction of lattice size caused by the smaller Sb^{3+}

radius compared to the Bi^{3+} during in-situ doping. The presence of Cs, Bi, Sb, and Br in CBSB-1 has been confirmed in the energy-dispersive spectroscopy (EDS) elemental mapping. To verify the precise incorporation of Sb into the system, the content of Bi and Sb was determined by an inductively coupled plasma-optical emission spectrometer (ICP-OES) with a ratio of 0.53:0.47, which is very close to the molecular formula, indicating the successful synthesis of CBSB-1 nanocrystals.

The phase structure of the samples was analyzed by XRD, as shown in Fig. 2(a). The powder X-ray diffraction (XRD) patterns of CBB and CSB are consistent with the standard cards PDF#44-0714 and PDF#77-1055, respectively. It can be seen that the XRD diffraction angle moves to the high field, indicating that the Sb content gradually increases. In addition, the chemical environmental difference of the samples was studied by X-ray photoelectron spectroscopy (XPS). Peaks of Sb can be observed in Fig. 2(b), confirming that Sb has been incorporated into the original lattice of CBB. To further investigate the effect of Sb^{3+} content on the electronic properties of CBSB-x, the binding energies of Cs 3d, Bi 4f, Sb 3d, and Br 3d were analyzed by high-resolution XPS with C1s (284.8 eV) corrected [13,23]. Fig. 2(c-f) shows that with the increase of the molar atomic ratio of Sb, the binding energies of Cs 3d and Bi 4f in CBSB-x decrease, indicating that the electron dispersion around Cs and Bi increases, which can be attributed to the improvement of $[Bi_2Br_9]^{3-}$ octahedral distortion [20,24,25]. The binding energy of Sb 3d shows a redshift opposite to that of Cs 3d and Bi 4f, confirming the contribution of Sb doping to the electronic environment in crystal structure. In addition, the binding energy of Br decreases first and then increases, where the blue shifts of Br $3d_{5/2}$ and Br $3d_{3/2}$ in CBSB-1 reaches the maximum (0.06 eV and 0.11 eV), suggesting that the increase of electron density around Br and the feasibility of electron transfer from Sb to Br, which is crucial for weakening the charge-hole pair strong
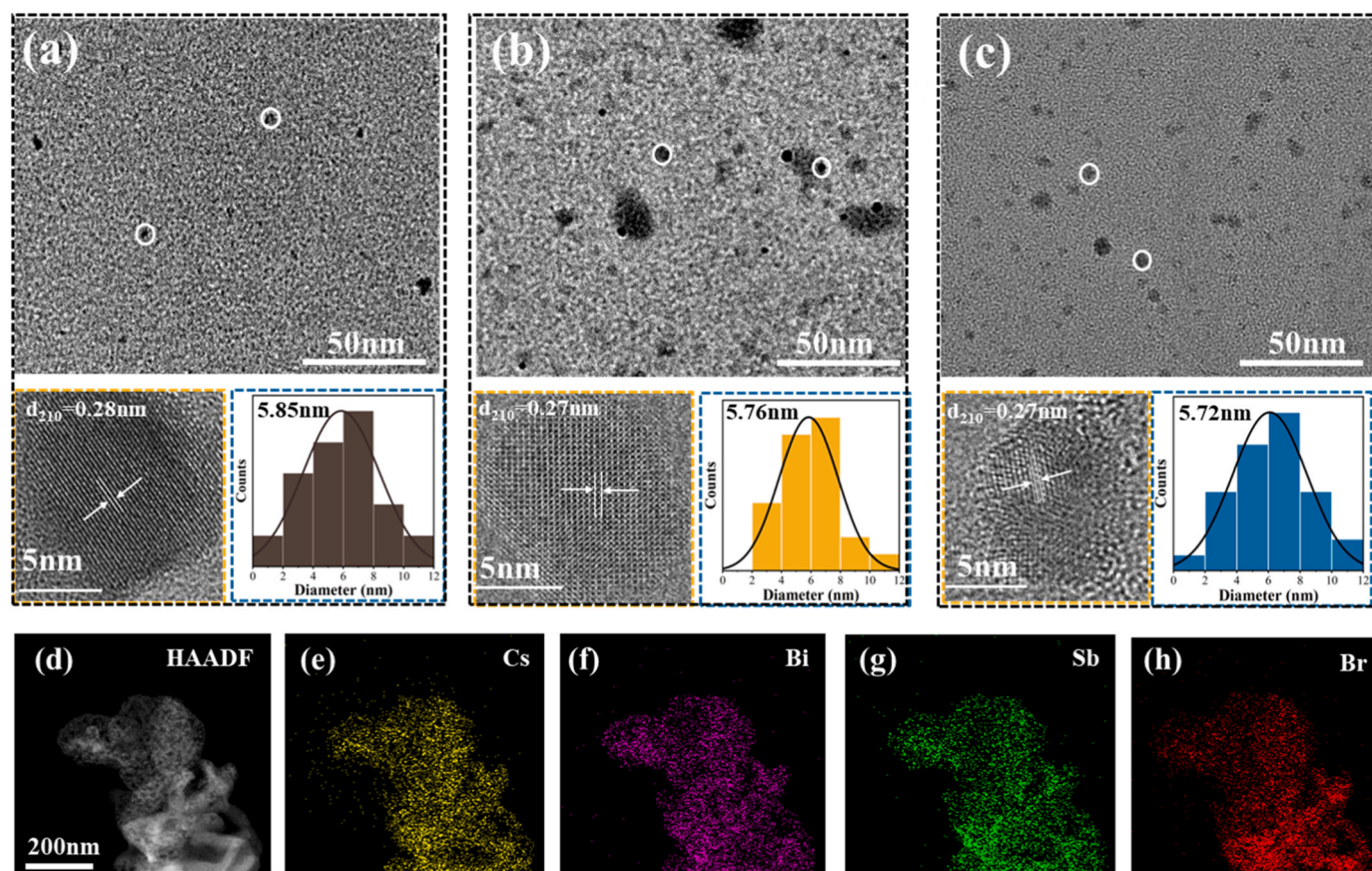

Fig. 1. Morphological characteristics of catalysts. TEM images, HRTEM images and Particle size distribution of CBB (a), CBSB-1 (b) and CSB (c). HAADF mapping (d) and EDS mapping images (e-h) of CBSB-1.
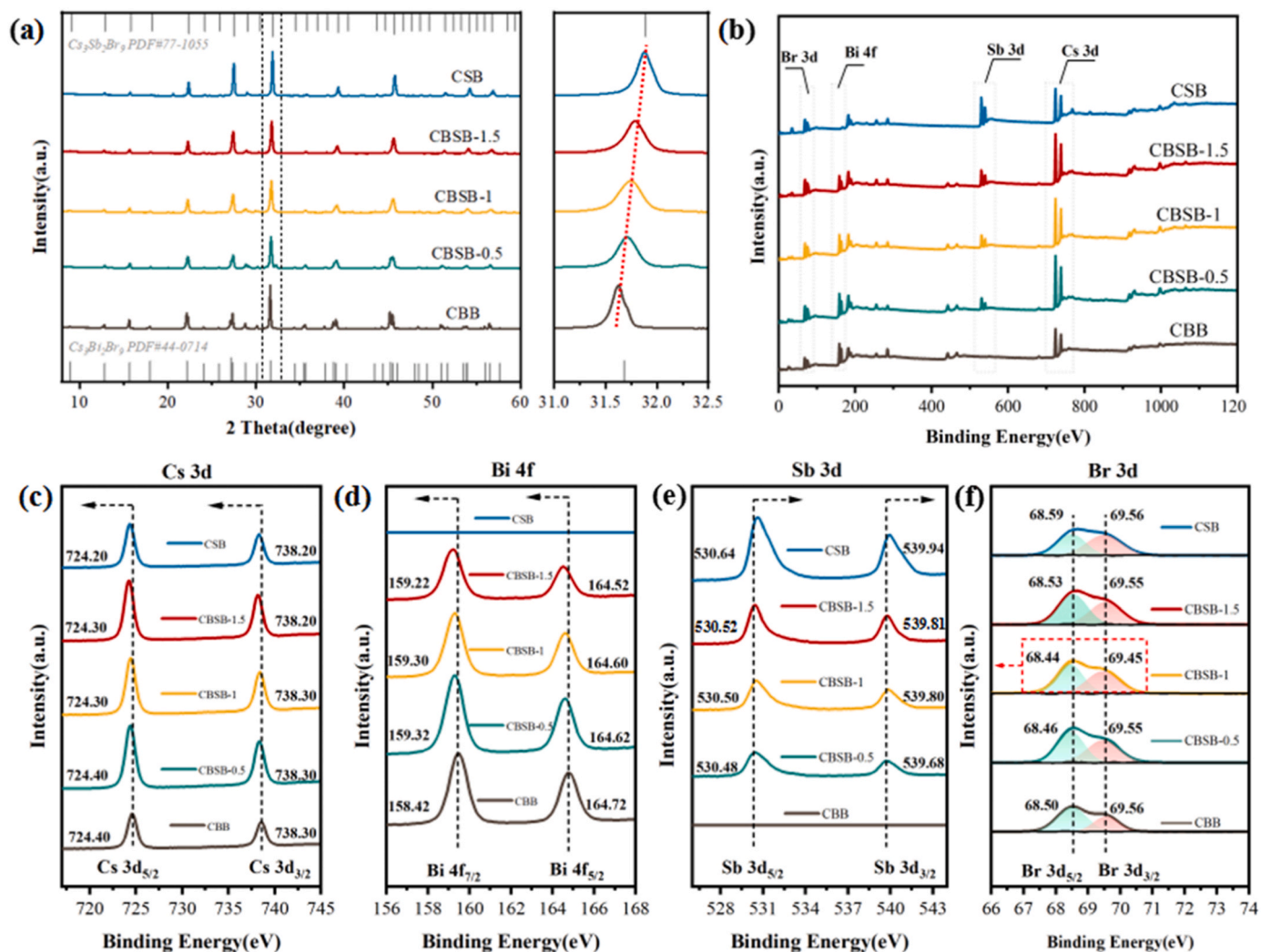
Fig. 2. XRD patterns (a) and XPS spectra (b) of CBB, CBSB-x and CSB. Cs 3d (c), Bi 4f (d), Sb 3d (e) and Br 3d (f) XPS spectra of CBB, CBSB-x and CSB.

localization around Bi and Br.

3.2. Band structure characteristics analysis

Ultraviolet-visible diffuse reflection (UV–vis DRS) spectra and valence-band (VB) XPS spectra were characterized to analyze the effect of Sb^{3+} content on the optical properties of the catalysts. As shown in Fig. 3(a), UV–vis DRS spectra results indicate that the absorption edge fluctuates accordingly with the change of Sb^{3+} content. Remarkably, the absorption edge of CBSB-1 extends from 495 nm to 569 nm, which is conducive to expanding the absorption range of visible light. The band gap widths of CBB, CBSB-x, and CSB were calculated by UV–vis DRS data. Compared with CBB (2.58 eV) and CSB (2.46 eV), the band gap widths of CBSB-1 were significantly reduced to 2.31 eV, which might be due to the hybridization effect between the atomic orbitals of Sb^{3+} and the valence or conduction atomic orbitals of CBB, further inducing the emergence of local energy levels. The spectrum edge of VB-XPS decreases from 1.82 eV to 1.47 eV with Sb doping, confirming the change of crystal VB top. Specifically, the conduction band of CBB is mainly contributed by the Bi 6p orbitals and Br 4p orbitals, in which the Bi 6p orbital in a semi-full state plays a major role in constituting the conduction band [22]. After the orbital hybridization of Sb and CBB, the new local energy level closer to the valence band is formed, resulting in the downward shift of the Fermi level, which improves the transport capacity of carriers, and further optimizes the optical properties and

catalytic activity of the catalysts.

3.3. CO$_2$ photoreduction activity assessments

The photoreducing activities of CBB, CBSB-x, and CSB to CO_2 were evaluated under the sunlight simulated by a 300 W Xenon lamp with an AM 1.5 G filter. Gas chromatograph (GC) was used to monitor the possible reaction products. Fig. 4(a) shows the production of CO and CH_4 after continuous irradiation for 3 h under 25 °C circulating water. It can be seen that the yield of CO and CH_4 after 3 h of the original CBB is 6.64 $\mu mol \cdot g^{-1}$ and 0.87 $\mu mol \cdot g^{-1}$, respectively, and the corresponding average yield is only 2.21 $\mu mol \cdot g^{-1} \cdot h^{-1}$ and 0.29 $\mu mol \cdot g^{-1} \cdot h^{-1}$. With the increase of the molar atomic ratio of Sb, the CO_2 reduction activity of the catalyst showed a significant increase. The CO and CH_4 yields of CBSB-1 are the highest, corresponding to 38.77 $\mu mol \cdot g^{-1}$ and 1.39 $\mu mol \cdot g^{-1}$, which were 5.84 and 1.60 times of those of CBB, respectively. Meanwhile, the CO selectivity of CBSB-1 increased from 88.37 % to 96.53 % compared with CBB, which can be attributed to the changes in electronic states caused by its distinctive bimetallic structure. However, as the atomic molar ratio of Sb continued to increase, the photocatalytic performance began to decline. When Bi was all replaced by Sb, the photocatalytic performance of CSB was reduced to the same level as that of CBB. Fig. 4(b) shows 5 consecutive 3 h-cycle experiments conducted under simulated sunlight irradiation. The results show that CBSB-1 exhibits a relatively constant CO yield, indicating that the catalyst has
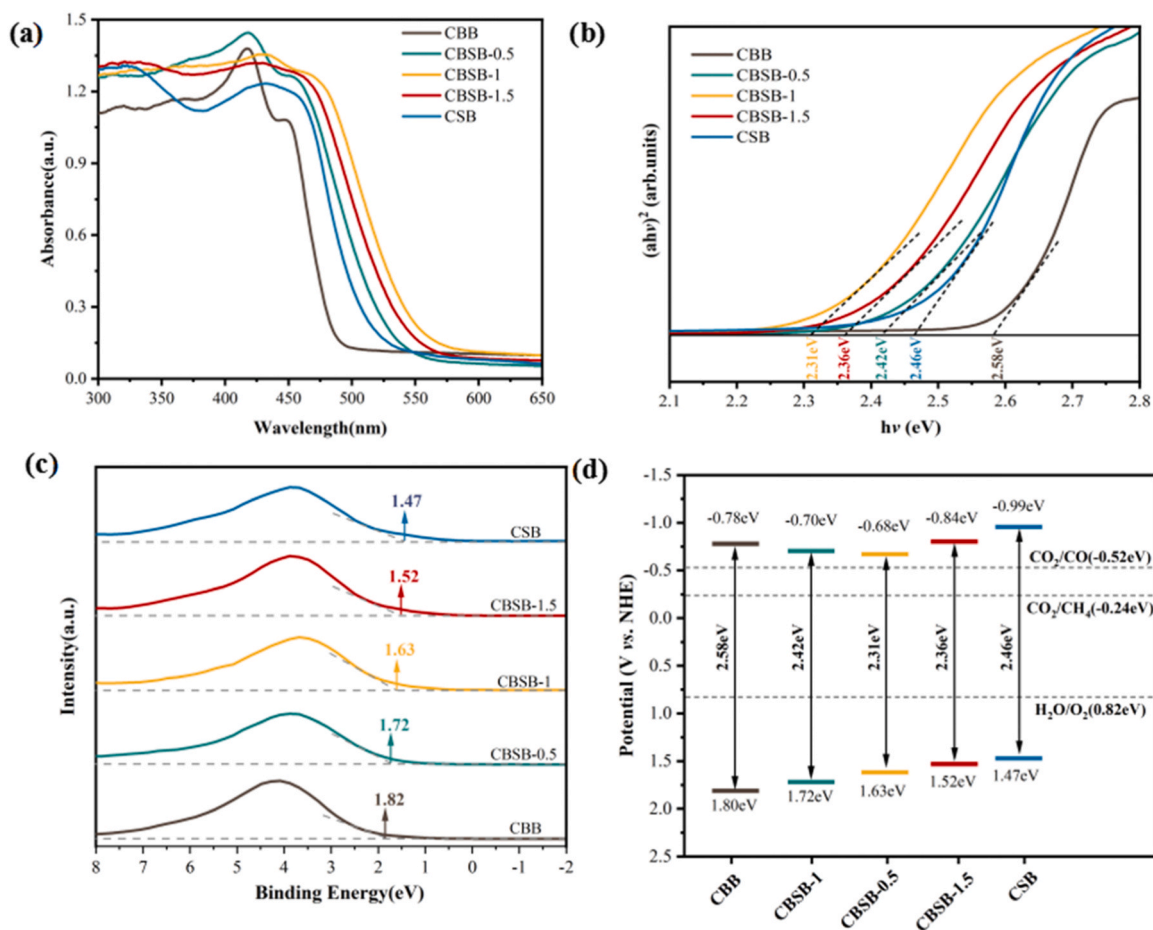
Fig. 3. UV–vis DRS spectra (a), $(\alpha h\nu)^2$ vs. light energy based on UV–vis DRS (b), VB-XPS spectra (c) and band structure (d) of CBB, CBSB-x and CSB.

stable catalytic performance under long-term illumination. To confirm the origin of CO, a controlling experiment was implemented with variables in check. CO was not produced in the absence of light or catalyst, indicating that both are necessary for photocatalytic reactions. Furthermore, the absence of CO signal in the presence of Ar as a reaction gas suggests that CO was exclusively generated via the decomposition of CO_2. Isotope labeling experiments with gas chromatography mass spectrometry (GC-MS) were conducted to elucidate the origin of the carbon source in the product. The detection of $m/z = 17$ and $m/z = 29$, corresponding to $^{13}CH_4$ and ^{13}CO species, respectively, indicates that they are derived from $^{13}CO_2$ substrates reduced by light, rather than from the decomposition of residual organics in the catalyst preparation [26].

3.4. Photophysical properties and electronic transmission abilities

The transient photocurrent response directly reflects the catalyst's ability to generate, transmit, and collect charge carriers, as shown in Fig. 5(a). The results indicate that CBSB-1 exhibits a higher photocurrent intensity than CBB and CSB, suggesting that it possesses superior photoresponse capabilities and photogenerated carrier transfer efficiency, which will result in more efficient conversion of photons into electrons and a faster reduction of CO_2 on the catalyst surface [27]. In addition, steady-state photoluminescence spectroscopy (PL) spectra and time-resolved photoluminescence spectroscopy (TRPL) spectra are essential methods for characterizing the structure and defects of catalysts. The PL spectra of CBB, CBSB-1, and CBB were analyzed in Fig. 5 (b). The low PL intensity of CBB is attributed to charge carriers recombination caused by a large number of internal defects, resulting in

increased energy loss for photogenerated electrons and holes, and thus reduced photoconversion efficiency of the catalyst [23,28]. The TRPL spectra were fitted with a double exponential function. As shown in Fig. 5(c), the macroscopic average carrier lifetime ($\tau_{average}$) in CBB, CBSB-1, and CSB are 13.67 ns , 30.95 ns and 19.34 ns, respectively, and the $\tau_{average}$ of CBSB-1 is significantly increased, which is conducive to improving the efficiency of excited electron transfer and accelerating the reaction process [29]. The effects of doping on the charge carrier non-radiative recombination (τ_1) and sub-bandgap state radiative recombination (τ_2) were further investigated [30]. Comparing the independent percentages of τ_1 and τ_2, it is found that the average macroscopic carrier lifetime $\tau_{average}$ of CBSB-1 increases, but the A_1 ratio decreases, indicating that the decrease of non-radiative recombination caused by bimetallic structures, suggesting that surface defects or traps of materials will be reduced, which will facilitate the separation and transfer of electrons and holes as well as actively promote surface catalytic reactions [31]. In addition, EPR spectra of CBB, CBSB-1, and CSB all exhibit a Lorentz line of $g = 2.01$, confirming that the electron states formed by the photoelectron-active region have spin resonance properties. The low spectral line intensity of CBSB-1 is an intuitive representation of its low defect state density, which is also one of the contributing factors to the photocatalytic activity [21]. External quantum efficiency (EQE) has been analyzed under specific spectra (Fig S2), and it can be seen that CBSB-1 exhibits higher EQE than CBB and CSB, indicating its high charge transfer efficiency and light conversion ability.

3.5. CO_2 photoreduction pathway and reaction mechanism

In order to further elucidate the possible mechanism of
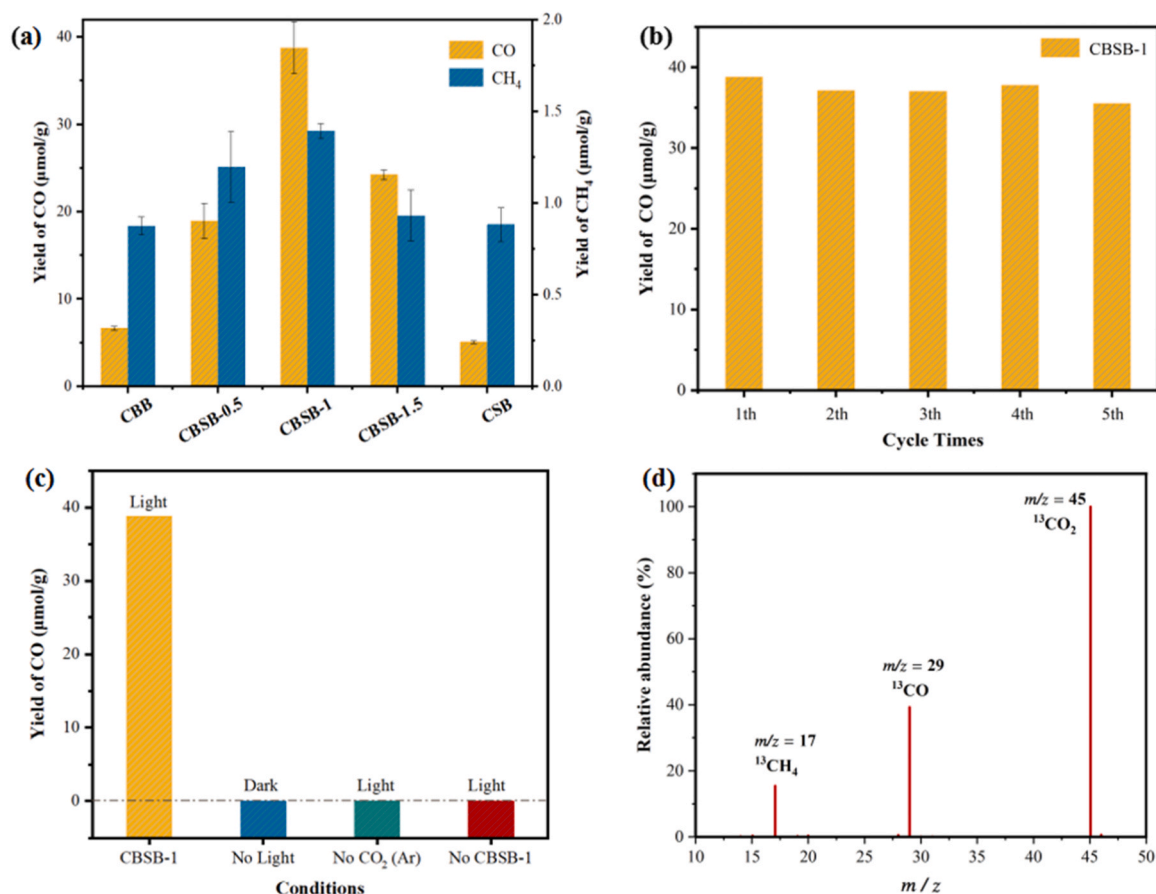
Fig. 4. Evaluation of CO_2 photoreduction activity. Yield of CO and CH_4 for 3 h of CBB, CBSB-x and CSB (a). Yield of CO for 3 h-cycle experiments of CBSB-1 at simulated sunlight (b). CO yield of CBSB-1 at different conditions (c). The GC- MS spectrum of photoreduction products over CBSB-1 using $^{13}CO_2$ as carbon source (d).

photoreduction of CO_2 by CBB, CBSB-1 and CSB, in-situ DRIFTS are used to record the variation of adsorption species and reaction intermediates on catalyst surface over time under dark and simulated sunlight respectively. As shown in Fig. 6(a-c), the peaks observed around 1648–1709 cm^{-1} and 1420 cm^{-1} in the dynamic infrared spectra can be attributed to the activated $^*CO_2$ and bicarbonate species (HCO_3^-) under dark conditions, confirming the dark adsorption and protonation of CO_2 on the catalyst surface [13,32]. Peaks occurring around 1514–1547 cm^{-1}, 1583 cm^{-1}, and 1740 cm^{-1} are assigned to monodentate carbonates (m-CO_3^{2-}), bidentate carbonates (b-CO_3^{2-}), and chelated bridge carbonates (c-CO_3^{2-}), which are key intermediates demonstrating CO_2 activation [33]. In addition, Fig. 6(a) and (b) exhibit the rapid saturation of intermediate species over a limited time compared to Fig. 6(c), indicating that compared to CSB, CBB and CBSB-1 have weaker adsorption capacity for b-CO_3^{2-}, reducing the risk of excessive accumulation of intermediate products and coverage of active sites. Fig. 6(d-e) illustrates the temporal evolution of surface intermediates under constant light radiation after deducting the dark adsorption background spectra collected at the 10th minute. Upon continuous illumination, the peak signals of $^*CO_2$ (1648–1709 cm^{-1}), m-CO_3^{2-} (1514–1547 cm^{-1}), and c-CO_3^{2-} (1740 cm^{-1}) increased, while the peak intensity signal of 1583 cm^{-1} decreased, indicating that b-CO_3^{2-} is rapidly consumed and transformed in the process of CO_2 reduction. Regrettably, as illustrated in Fig. 6(d), the accumulation of b-CO_3^{2-} begins at the 10th minute, possibly due to the fact that the conversion rate of b-CO_3^{2-} in CBB is lower than its generation rate. Furthermore, as shown in Fig. 6(f), the peak of b-CO_3^{2-} continues to increase after illumination, potentially attributed to the strong adsorption capacity of CSB. Both of these situations will lead to the occupation of active sites by

intermediate species, resulting in a decrease in reaction rate [13]. In contrast to CBB and CSB, CBSB-1 exhibits a continuous negative peak near 1583 cm^{-1}, illustrating that b-CO_3^{2-} undergoes rapid optical evolution on the catalyst surface, which might be related to the high charge carrier separation efficiency and charge transfer rate of CBSB-1. After sustained light exposure, the peak signal of monodentate formate (m-$HCOO^-$) (1617–1619 cm^{-1}) is enhanced, and it is considered to be a key species in the conversion of CO_2 to CO [34,35]. In addition, the wide peaks of low intensity appearing in the low wave-number regions of 1068 cm^{-1} and 1197 cm^{-1} increasing with time can be assigned as the intermediate CH_XO peaks for the formation of CH_4 [21,36].

The adsorption energy of CO_2 plays a pivotal role in dictating the catalytic adsorption efficiency, owing to its involvement in the initial step of the activation process. Therefore, CBB, CBSB-1, and CSB models have been established to analyze their connectivity with CO_2, as shown in Fig. 7. In order to demonstrate the contribution of Sb doping to improving the photocatalytic performance of CO_2, the Bi-Br-Bi, Bi-Br-Sb, and Sb-Br-Sb interfaces were cut and exposed as the main adsorption sites for CO_2. Fig. S3 shows the configuration of CO_2 at different adsorption sites. The optimal adsorption configuration revealed that the E_{ads} of CBSB-1 (-17.11 kJ·mol^{-1}) was higher than that of CBB (-16.75 kJ·mol^{-1}) and CSB (-16.35 kJ·mol^{-1}). Simultaneously, CO_2 exhibits the largest bond angle change during the adsorption process of CBSB-1, bending from 180° to 178.97°, indicating that CO_2 is more easily adsorbed on the Bi-Br-Sb interface. To further analyze the adsorption mechanism of CO_2 on the catalyst surface, the charge density difference, which is the direct data of electron flow direction after atomic interaction, is employed. The maximum negative values of the surface charge differential density along the X axis are -1.5×10^{-4}
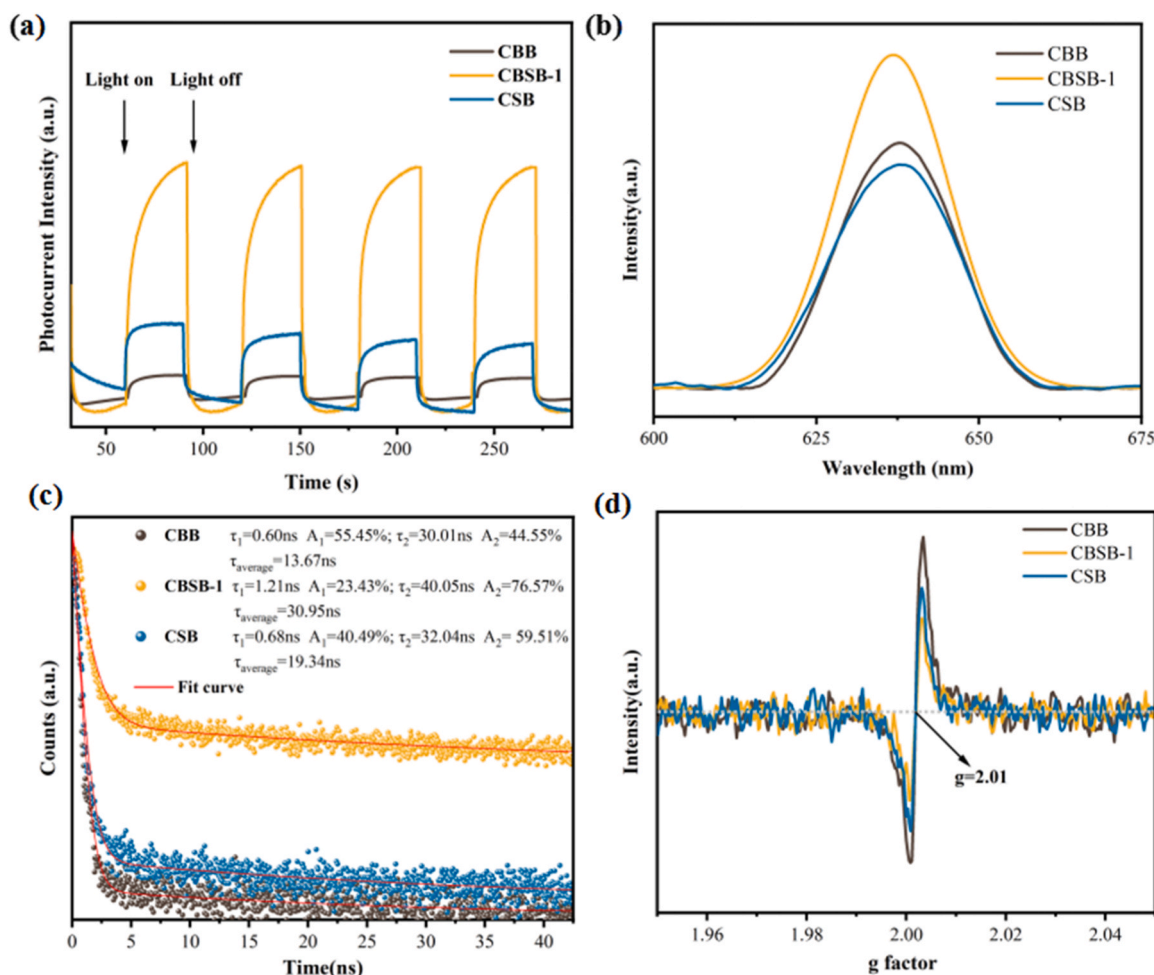
Fig. 5. The transient photocurrent responses plot (a), PL spectra (b), TRPL (c) and EPR (d) plots of CBB, CBSB-1 and CSB.

e·Å^{-1}, -2.2×10^{-4} e·Å^{-1} and -1.1×10^{-4} e·Å^{-1}, respectively, representing the maximum charge consumption of the Bi-Br-Bi, Bi-Br-Sb, and Sb-Br-Sb interfaces [37]. The maximum positive values are 0.6×10^{-4} e·Å^{-1}, 1.1×10^{-4} e·Å^{-1}, and 0.7×10^{-4} e·Å^{-1}, respectively, indicating the amount of charge clustering in CO_2. The significant numerical fluctuations suggest that the abundant charge transfer between CO_2 and CBSB-1, which is conducive to further activation reactions.

The Bader charge analysis of CBB, CBSB-1, and CSB has been calculated, as shown in Table S1. It can be seen that the incorporation of Sb changes the charge distribution and increases the electron density distribution around Bi and Br, which is conducive to promoting the adsorption and activation of CO_2 at the Bi and Br sites. In addition, the PDOS for CBB, CBSB-1, and CSB and p-band centers for Br are also provided in Fig. S4 and Fig. S5. It can be seen that the incorporation of Sb will significantly reduce the contribution of Bi atoms to the conduction band, which is conducive to promoting charge transfer around Bi and increasing the degree of charge delocalization. At the same time, the p-band center of Br shifts to the right with the incorporation of Sb, which is greatly beneficial for improving the contribution of Br sites.

Based on in-situ DRIFTS and DFT information, the free energy of transition states corresponding to key intermediates, *CO_2, b-CO_3*, HCOO*, and CO*, was calculated, and the reaction pathway was reasonably predicted, as shown in Fig. 8(a) and (b). Firstly, H_2O is adsorbed on the catalyst surface and activated to OH by Bi or Sb Lewis acid sites, and the OH on the surface bonds with CO_2 to form b-CO_3^{2-} [13, 38]. The step I is a spontaneous process, and the adsorption site of b-CO_3^{2-} on CBSB-1 is the same as that on CBB, which is consistent with the stable chemical environment represented by the unshifted peak position in

in-situ DRIFTS. In addition, the lower free energy of CBSB-1 compared to CBB indicates that Sb is a co-catalytic site optimizing the catalytic activity of Bi sites [39]. After light radiation, photogenerated electrons collaborate with protons to convert b-CO_3^{2-} into HCOO$^-$, and the C–H and C–O bonds of HCOO$^-$ break under further proton attack. The step II is the rate-determining step in the photoreduction of CO_2 to CO. The free energy barrier ΔG of CBB, CBSB-1 and CSB in step II is 3.38 eV, 3.26 eV and 4.63 eV, respectively, confirming that the bimetallic configuration of Bi-Sb can diminish the reaction energy. CO is reduced at free energies of 0.52 eV, -0.62 eV, and 0.93 eV on CBB, CBSB-1, and CSB, illustrating that the CO energy barrier of CBSB-1 is significantly reduced, which is greatly beneficial for improving its photoreduction performance.

4. Conclusion

A series of perovskite nanocrystals with diverse Bi/Sb ratios have been successfully synthesized and exhibit exceptional activity and selectivity in CO_2 photoreduction. The CO conversion rate of CBSB-1 is as high as 38.77 μmol·g^{-1}, which is 5.84 times that of CBB. The CO selectivity of CBSB-1 reached 96.53 % and remained stable over 5 cycles. Compared with original CBB, CBSB-1 can reduce charge carrier nonradiative recombination and increase charge transfer efficiency. Serving as a co-catalytic site, Sb promotes the rapid kinetic evolution of b-CO_3^{2-} at the Bi-Br-Sb interface of CBSB-1, while reducing the reaction energy barrier and accelerating CO spillover through by improvement of electronic structure. This work provides a new paradigm for future alternative options of perovskite in the CRR field.
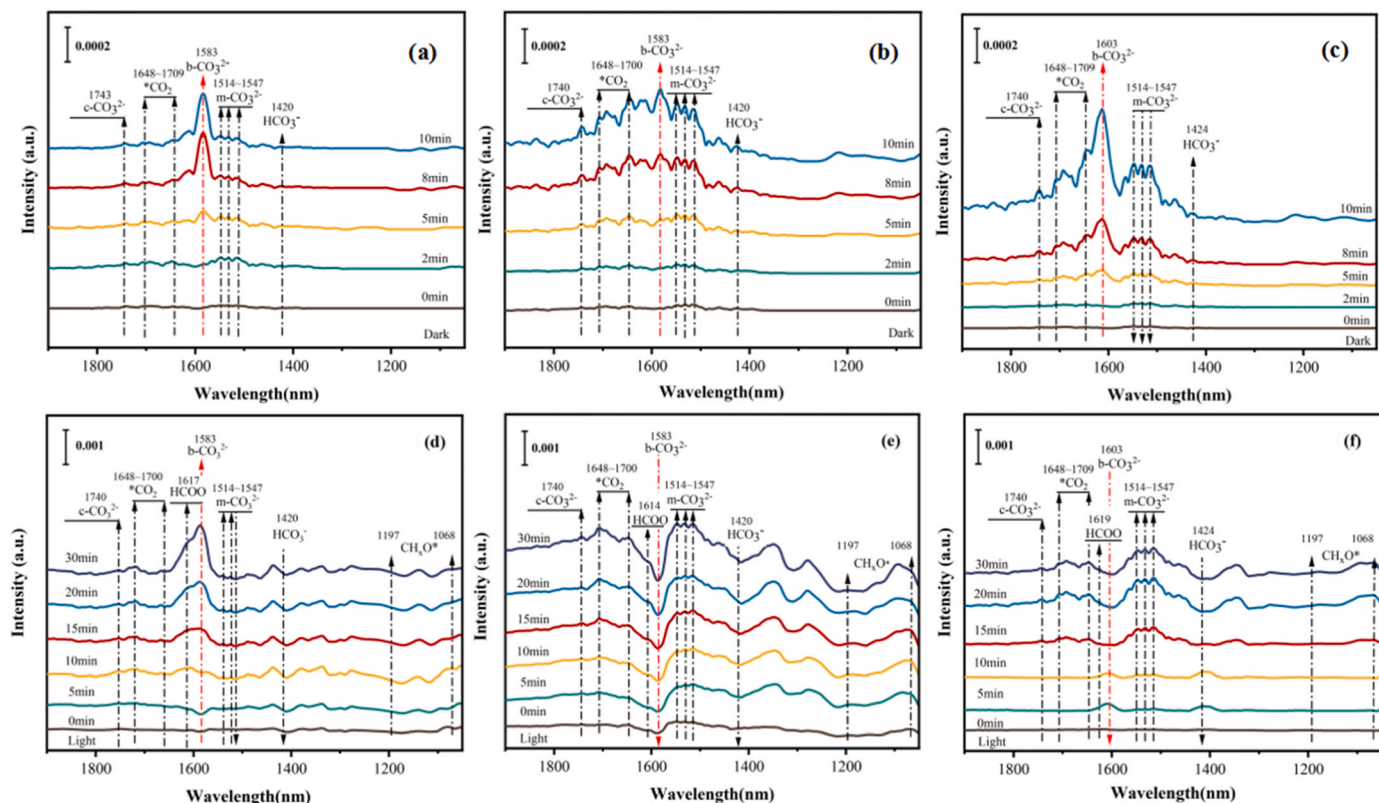
Fig. 6. In situ DRIFTS under dark condition and constant simulated sunlight condition of CBB (a, d), CBSB-1 (b, e) and CSB (c, f).
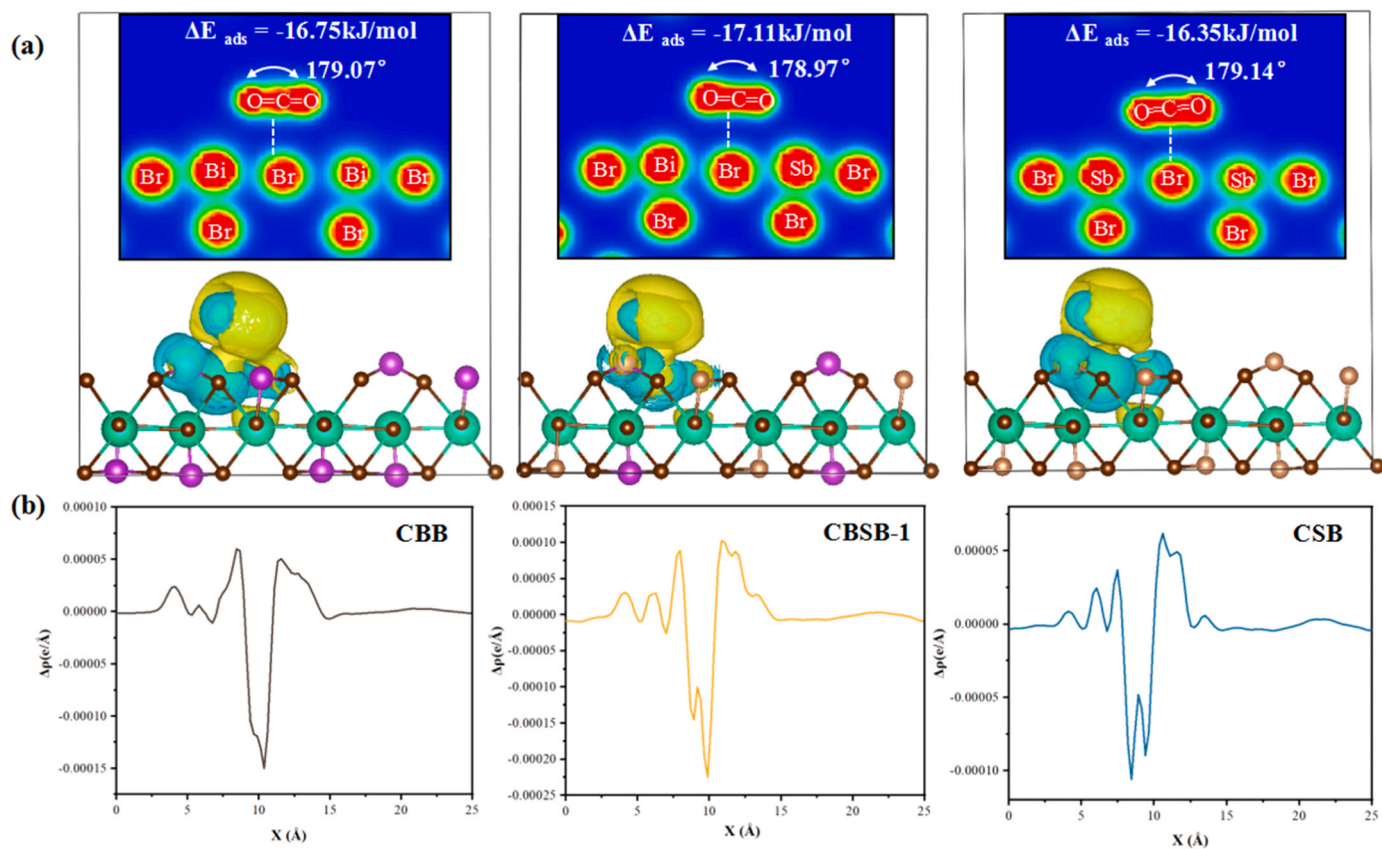

Fig. 7. The CO_2 adsorption configurations, corresponding electron localization function and charge density difference on CBB, CBSB-1, CSB (a). Plane-averaged charge density difference of CBB, CBSB-1 and CSB (b).
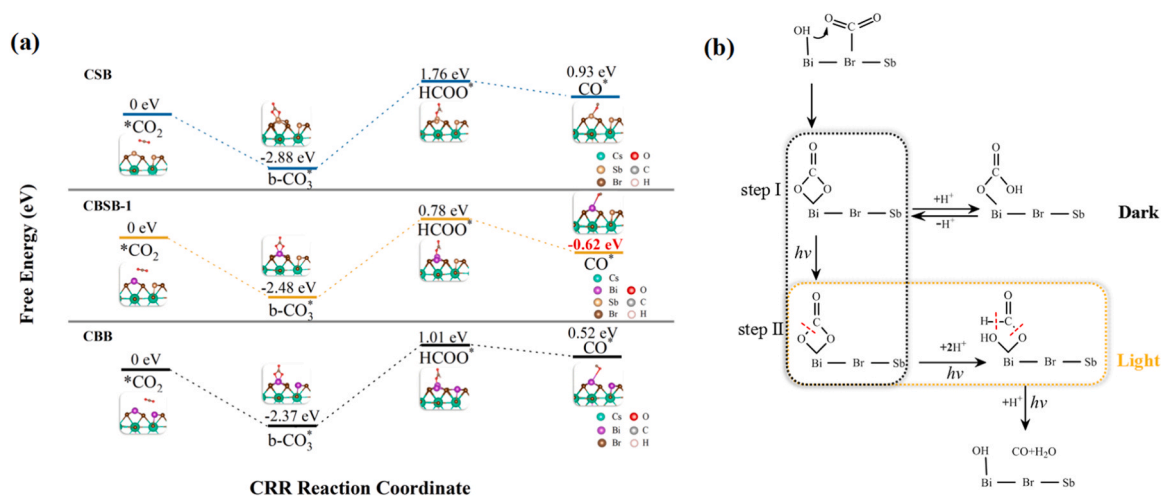
Fig. 8. Free energy of transition state in CO_2 photoreduction by CBB, CBSB-1 and CSB (a). The hypothesized mechanism of CO_2 photoreduction reaction on the surface of CBSB-1 (b).

CRediT authorship contribution statement

Jie Tian: Conceptualization, Methodology, Investigation, Writing - original draft. **Zhijian Wang:** Writing - review & editing, Supervision. **Yaqin Hou:** Writing - review & editing, Supervision, Resources. **Yatao Yang:** Visualization, Data Curation. **Haijun Chen:** Investigation, Software support. **Zhanggen Huang:** Conceptualization, Supervision, Resources.

Declaration of Competing Interest

The authors declare that they have no known competing financial interests or personal relationships that could have appeared to influence the work reported in this paper.

Data availability

Data will be made available on request.

Acknowledgements

Appendix A. Supporting information

Supplementary data associated with this article can be found in the online version at doi:10.1016/j.apcatb.2023.123272.

References

[1] O.S. Bushuyev, P. De Luna, C.T. Dinh, L. Tao, G. Saur, J. van de Lagemaat, S. O. Kelley, E.H. Sargent, What should we make with CO_2 and how can we make it? Joule 2 (5) (2018) 825–832.

[2] K. Rennert, F. Errickson, B.C. Prest, L. Rennels, R.G. Newell, W. Pizer, C. Kingdon, J. Wingenroth, R. Cooke, B. Parthum, D. Smith, K. Cromar, D. Diaz, F.C. Moore, U. K. Muller, R.J. Plevin, A.E. Raftery, H. Sevcikova, H. Sheets, J.H. Stock, T. Tan, M. Watson, T.E. Wong, D. Anthoff, Comprehensive evidence implies a higher social cost of CO_2, Nature 610 (7933) (2022) 687–692.

[3] S.C. Sarma, J. Barrio, A. Bagger, A. Pedersen, M. Gong, H. Luo, M. Wang, S. Favero, C.X. Zhao, Q. Zhang, A. Kucernak, M.M. Titirici, I.E.L. Stephens, Reaching the fundamental limitation in CO_2 reduction to CO with single atom catalysts, Adv. Funct. Mater. (2023), 2302468.

[4] Y. Qiao, J.J. Bailey, Q. Huang, X. Ke, C. Wu, Potential photo-switching sorbents for CO_2 capture – a review, Renew. Sustain. Energy Rev. 158 (2022), 112079.

[5] W. Bi, Y. Hu, N. Jiang, L. Zhang, H. Jiang, X. Zhao, C. Wang, C. Li, Ultra-fast construction of plaque-like Li_2TiO_3/TiO_2 heterostructure for efficient gas-solid phase CO_2 photoreduction, Appl. Catal. B: Environ. 269 (2020), 118810.

[6] X. Chen, C. Peng, W. Dan, L. Yu, Y. Wu, H. Fei, Bromo- and iodo-bridged building units in metal-organic frameworks for enhanced carrier transport and CO_2 photoreduction by water vapor, Nat. Commun. 13 (1) (2022) 4592.

[7] J. Zhu, W. Shao, X. Li, X. Jiao, J. Zhu, Y. Sun, Y. Xie, Asymmetric triple-atom sites confined in ternary oxide enabling selective CO_2 photothermal reduction to acetate, J. Am. Chem. Soc. 143 (43) (2021) 18233–18241.

[8] W. Tu, Y. Zhou, Z. Zou, Photocatalytic conversion of CO_2 into renewable hydrocarbon fuels: state-of-the-art accomplishment, challenges, and prospects, Adv. Mater. 26 (27) (2014) 4607–4626.

[9] J. Fu, S. Ramesh, J.W. Melvin Lim, T.C. Sum, Carriers, quasi-particles, and collective excitations in halide perovskites, Chem. Rev. 123 (13) (2023) 8154–8231.

[10] J. Chen, C. Dong, H. Idriss, O.F. Mohammed, O.M. Bakr, Metal halide perovskites for solar-to-chemical fuel conversion, Adv. Energy Mater. 10 (13) (2019).

[11] T. Roh, H. Zhu, W. Yang, A. Liu, Y.Y. Noh, Ion migration induced unusual charge transport in tin halide perovskites, ACS Energy Lett. 8 (2) (2023) 957–962.

[12] S.S. Bhosale, A.K. Kharade, E. Jokar, A. Fathi, S.M. Chang, E.W. Diau, Mechanism of photocatalytic CO_2 reduction by Bismuth-based perovskite nanocrystals at the gas-solid interface, J. Am. Chem. Soc. 141 (51) (2019) 20434–20442.

[13] J. Sheng, Y. He, J. Li, C. Yuan, H. Huang, S. Wang, Y. Sun, Z. Wang, F. Dong, Identification of halogen-associated active sites on Bismuth-based perovskite quantum dots for efficient and selective CO_2-to-CO photoreduction, ACS Nano 14 (10) (2020) 13103–13114.

[14] B. Yang, J. Chen, F. Hong, X. Mao, K. Zheng, S. Yang, Y. Li, T. Pullerits, W. Deng, K. Han, Lead-free, air-stable all-inorganic cesium Bismuth Halide perovskite nanocrystals, Angew. Chem. Int. Ed. Engl. 56 (41) (2017) 12471–12475.

[15] M. Leng, Y. Yang, K. Zeng, Z. Chen, Z. Tan, S. Li, J. Li, B. Xu, D. Li, M.P. Hautzinger, Y. Fu, T. Zhai, L. Xu, G. Niu, S. Jin, J. Tang, All-inorganic Bismuth-based perovskite quantum dots with bright blue photoluminescence and excellent stability, Adv. Funct. Mater. 28 (1) (2017).

[16] X. Yang, Y.H. Huang, X.D. Wang, W.G. Li, D.B. Kuang, A-site diamine cation anchoring enables efficient charge transfer and suppressed ion migration in bi-based hybrid perovskite single crystals, Angew. Chem. Int. Ed. Engl. 61 (29) (2022), e202204663.

[17] H. Wang, W. Liu, X. He, P. Zhang, X. Zhang, Y. Xie, An excitonic perspective on low-dimensional semiconductors for photocatalysis, J. Am. Chem. Soc. 142 (33) (2020) 14007–14022.

[18] Q.M. Sun, J.J. Xu, F.F. Tao, W. Ye, C. Zhou, J.H. He, J.M. Lu, Boosted inner surface charge transfer in perovskite nanodots@mesoporous titania frameworks for efficient and selective photocatalytic CO_2 reduction to methane, Angew. Chem. Int. Ed. 61 (20) (2022).

[19] Z. Huang, J.X. Liang, D. Tang, Y. Chen, W. Qu, X. Hu, J. Chen, Y. Dong, D. Xu, D. Golberg, J. Li, X. Tang, Interplay between remote single-atom active sites triggers speedy catalytic oxidation, Chem 8 (11) (2022) 3008–3017.

[20] M. Shi, G. Li, W. Tian, S. Jin, X. Tao, Y. Jiang, E.A. Pidko, R. Li, C. Li, Understanding the effect of crystalline structural transformation for lead-free inorganic halide perovskites, Adv. Mater. 32 (31) (2020), e2002137.

[21] J. Pi, X. Jia, Z. Long, S. Yang, H. Wu, D. Zhou, Q. Wang, H. Zheng, Y. Yang, J. Zhang, J. Qiu, Surface and defect engineering coupling of halide double perovskite $Cs_2NaBiCl_6$ for efficient CO_2 photoreduction, Adv. Energ. Mater. 12 (43) (2022) 2202074.

[22] M. Shi, H. Zhou, W. Tian, B. Yang, S. Yang, K. Han, R. Li, C. Li, Lead-free B-site bimetallic perovskite photocatalyst for efficient benzylic C–H bond activation, Cell. Rep. Phys. Sci. 2 (12) (2021), 100656.

[23] G. Chen, P. Wang, Y. Wu, Q. Zhang, Q. Wu, Z. Wang, Z. Zheng, Y. Liu, Y. Dai, B. Huang, Lead-free halide perovskite $Cs_3Bi_{2x}Sb_{2-2x}I_9$ ($x \approx 0.3$) possessing the photocatalytic activity for hydrogen evolution comparable to that of $(CH_3NH_3)PbI_3$, Adv. Mater. 32 (39) (2020) e2001344.

[24] F. Liu, J. Jiang, Y. Zhang, C. Ding, T. Toyoda, S. Hayase, R. Wang, S. Tao, Q. Shen, Near-infrared emission from tin-lead (Sn-Pb) alloyed perovskite quantum dots by sodium doping, Angew. Chem. Int. Ed. 59 (22) (2020) 8421–8424.

[25] K.M. McCall, C.C. Stoumpos, S.S. Kostina, M.G. Kanatzidis, B.W. Wessels, Strong electron–phonon coupling and self-trapped excitons in the defect halide perovskites $A_3M_2I_9$ (A = Cs, Rb; M = Bi, Sb), Chem. Mater. 29 (9) (2017) 4129–4145.

[26] X. Wang, Z. Wang, Y. Li, J. Wang, G. Zhang, Efficient photocatalytic CO_2 conversion over 2D/2D Ni-doped $CsPbBr_3/Bi_3O_4Br$ Z-scheme heterojunction: critical role of Ni doping, boosted charge separation and mechanism study, Appl. Catal. B: Environ. 319 (2022) 121895.

[27] D. Wu, B. Huo, Y. Huang, X. Zhao, J. Yang, K. Hu, X. Mao, P. He, Q. Huang, X. Tang, Synthesis of stable lead-free $Cs_3Sb_2(Br_xI_{1-x})_9$ ($0 \leq x \leq 1$) perovskite nanoplatelets and their application in CO_2 photocatalytic reduction, Small 18 (12) (2022) e2106001.

[28] X.D. Wang, Y.H. Huang, J.F. Liao, Z.F. Wei, W.G. Li, Y.F. Xu, H.Y. Chen, D. B. Kuang, Surface passivated halide perovskite single-crystal for efficient photoelectrochemical synthesis of dimethoxydihydrofuran, Nat. Commun. 12 (1) (2021) 1202.

[29] W. Xue, H. Sun, X. Hu, X. Bai, J. Fan, E. Liu, UV–VIS–NIR-induced extraordinary H_2 evolution over $W_{18}O_{49}/Cd_{0.5}Zn_{0.5}S$: surface plasmon effect coupled with S-scheme charge transfer, Chin. J. Catal. 43 (2) (2022) 234–245.

[30] C.C. Lin, T.R. Liu, S.R. Lin, K.M. Boopathi, C.H. Chiang, W.Y. Tzeng, W.C. Chien, H. S. Hsu, C.W. Luo, H.Y. Tsai, H.A. Chen, P.C. Kuo, J. Shiue, J.W. Chiou, W.F. Pong, C.C. Chen, C.W. Chen, Spin-polarized photocatalytic CO_2 reduction of Mn-doped perovskite nanoplates, J. Am. Chem. Soc. 144 (34) (2022) 15718–15726.

[31] X. Zhang, X. Li, L. Tao, Z. Zhang, H. Ling, X. Fu, S. Wang, M.J. Ko, J. Luo, J. Chen, Y. Li, Precise control of crystallization and phase-transition with green anti-solvent in wide-bandgap perovskite solar cells with open-circuit voltage exceeding 1.25 V, Small 19 (22) (2023) 2208289.

[32] J. Sheng, Y. He, M. Huang, C. Yuan, S. Wang, F. Dong, Frustrated Lewis pair sites boosting CO_2 photoreduction on Cs_2CuBr_4 perovskite quantum dots, ACS Catal. 12 (5) (2022) 2915–2926.

[33] D. Wu, C. Wang, B. Huo, K. Hu, X. Mao, Z. Geng, Q. Huang, W. Zhang, J. Zeng, X. Tang, Photo- and electrocatalytic CO_2 reduction based on stable lead-free perovskite Cs_2PdBr_6, Energy Environ. Mater. (2022).

[34] Y. Duan, Y. Wang, W. Zhang, J. Zhang, C. Ban, D. Yu, K. Zhou, J. Tang, X. Zhang, X. Han, L. Gan, X. Tao, X. Zhou, Simultaneous CO_2 and H_2O activation via integrated Cu single atom and N vacancy dual-site for enhanced CO photo-production, Adv. Funct. Mater. (2023) 2301729.

[35] D. Li, S. Jin, Z. Wang, Z. Jiang, F. Xiong, J. Wang, M. Zhu, Revealing the gas sensitive stability of formate species during CO_2 hydrogenation, Catal. Sci. Technol. 13 (11) (2023) 3226–3230.

[36] X. Yang, X. Lan, Y. Zhang, H. Li, G. Bai, Rational design of MoS_2@COF hybrid composites promoting C-C coupling for photocatalytic CO_2 reduction to ethane, Appl. Catal. B: Environ. 325 (2023), 122393.

[37] J. Di, X. Zhu, G. Hao, C. Zhu, H. Chen, Q. Liu, R. Duan, H. Hu, Y. Zhang, J. Xiong, R. Long, J. Xia, Y.X. Weng, W. Jiang, Z. Liu, Vacancy pair-induced charge rebalancing with surface and interfacial dual polarization for CO_2 photoreduction, ACS Catal. 12 (24) (2022) 15728–15736.

[38] L. Wang, W. Chen, D. Zhang, Y. Du, R. Amal, S. Qiao, J. Wu, Z. Yin, Surface strategies for catalytic CO_2 reduction: from two-dimensional materials to nanoclusters to single atoms, Chem. Soc. Rev. 48 (21) (2019) 5310–5349.

[39] H. Xu, L. Zhu, Y. Nan, Y. Xie, D. Cheng, Revisit the role of metal dopants in enhancing the selectivity of Ag-catalyzed ethylene epoxidation: optimizing oxophilicity of reaction site via cocatalytic mechanism, ACS Catal. 11 (6) (2021) 3371–3383.